Analysis of Chemically Reacting Transport Phenomena in an Anode Duct of Intermediate Temperature SOFCs

Jinliang Yuan

Bengt Sundén[1]
e-mail: bengt.sunden@vok.lth.se

Department of Energy Sciences,
Lund Institute of Technology,
Box 118, 22100 Lund, Sweden

The internal reforming and electrochemical reactions appear in the porous anode layer, and may lead to inhomogeneous temperature and gas species distributions according to the reaction kinetics. In this study, a fully three-dimensional calculation method has been further developed to simulate and analyze chemically reacting transport processes in a thick anode duct. The composite duct investigated consists of a porous anode, the fuel flow duct and solid current connector. Momentum and heat transport together with gas species equations have been solved by coupled source terms and variable thermophysical/transport properties of the fuel gas mixture. Furthermore, the heat transfer due to the fuel gas diffusion is implemented into the energy balance based on multicomponent diffusion models. The fuel cell conditions such as the combined thermal boundary conditions on solid walls, mass balances (generation and consumption) associated with the various reactions, and gas permeation between the porous anode and flow duct are applied in the analysis. Simulation results show that the internal reforming and the electrochemical reactions, and cell operating conditions are significant for species distribution, fuel gas transport and heat transfer in the subdomains of the anode. [DOI: 10.1115/1.2173662]

Keywords: analysis, chemical reacting, transport phenomena, porous anode, intermediate temperature, solid oxide fuel cell (SOFC)

1 Introduction

During recent years, one of the new trends is to reduce the operating temperature of solid oxide fuel cells (SOFCs) to a moderate range (from 1000°C to 800°C) by employing a thick porous layer (1.5–2 mm) as the supporting structure [1–4]. The size of the porous anode for this new design is bigger than that of the flow duct in terms of thickness and cross-sectional area. The transport rate of fuel gases to the active surface for electrochemical reactions is controlled by various parameters, such as porous microstructure (i.e., pore size, permeability, volume percent porosity of the employed porous layer), pressure gradient between the fuel flow duct and the porous anode, gas composition and inlet conditions, etc. [5–7].

For the case of pure hydrogen being employed as a fuel, it is true that part of H_2 is consumed while water vapor (H_2O) is generated during the electrochemical reaction. This is simulated as a mass suction and injection V_m (or $\mathrm{Re}_m = V_m D_h / \nu$), respectively, at the active wall on the anode side [6,7]. If hydrocarbon fuels are used as the fuels, it is a fact that the heat required to keep internal steam reforming can be provided by the electrochemical reactions in SOFCs. There are several advantages to have internal steam reforming of employed hydrocarbon fuels, for instances, the energy conversion efficiency will be much higher, and this benefit does not appear if the pure hydrogen is considered as the fuel. Moreover, close coupling of the internal reforming and the electrochemical reactions at the anode gives good heat transfer. Furthermore, hydrogen and CO are utilized by the cell as soon as they are produced by the reforming reaction, and the steam produced by the electrochemical reaction can be used in the reforming reaction as well [8]. However, most of the internal reforming reaction takes place in the porous anode next to the fuel gas flow duct due to the high methane conversion rate, and very little methane reaches the active surface between the electrolyte and the porous anode. The endothermic internal reforming reaction and the exothermic electrochemical reactions are separated, and consequently may lead to big temperature gradients in the porous layer.

There is a need to deeply understand the physical mechanisms and effects of the chemical reactions on the transport processes in the anode. To extend our previous studies [5–7], a fully three-dimensional numerical calculation procedure has been further developed to include the internal reforming reactions in the reduced temperature SOFC anode duct. The extension includes the oxidation and the shift reactions of CO at the active surface and the porous anode, respectively. The duct under investigation includes the porous anode, fuel gas flow duct and the solid interconnects. By calculating fuel gas species, the mass/heat generation and consumption related to the internal reforming and the electrochemical reactions have been identified and applied in the study. Moreover, the variable thermal-physical properties and transport parameters of the fuel gas mixture have also been taken into account. Furthermore, the heat transfer due to the fuel gas diffusion is implemented into the energy balance based on multicomponent diffusion models. One of the objectives of this paper is to develop such a calculation method to understand various reactions and the effects on various transport processes in the anode ducts of ITSOFCs.

2 Problem Statement and Equations

2.1 Chemical Reactions. Internal reforming reaction occurs in the porous anode region adjacent to the place where the electrochemical reaction appears, and the heat from the fuel cell electrochemical reactions is supplied for the reforming reaction by

[1]Corresponding author.

Manuscript received March 8, 2005; final manuscript received August 17, 2005. Review conducted by Nigel M. Sammes.

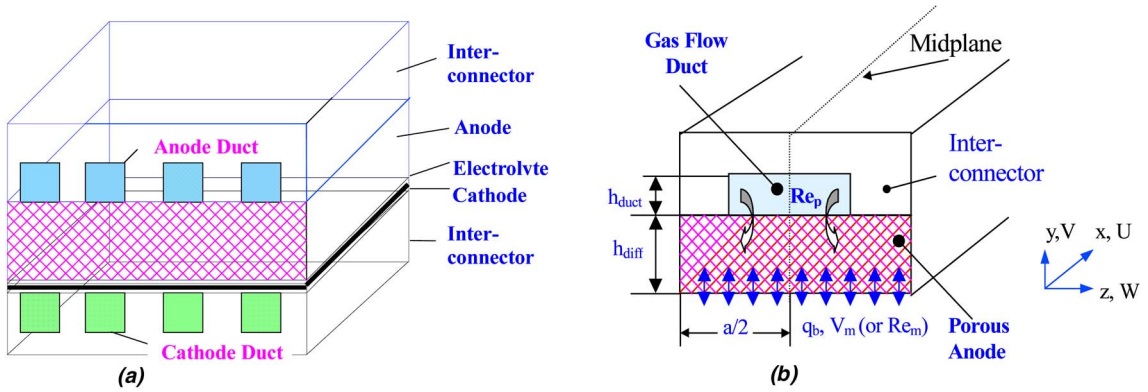

Fig. 1 (*a*) **Structure of a unit cell;** (*b*) **schematic drawing of a composite anode duct in ITSOFCs**

internal heat transfer with minimal losses.

Methane and carbon monoxide can be internally reformed into H_2 by the following reactions:

$$CH_4 + H_2O \rightarrow CO + 3H_2 \quad \Delta H_{1000\ K} = 226\ \text{kJ/mol} \tag{1}$$

$$CO + H_2O \rightarrow CO_2 + H_2 \quad \Delta H_{1000\ K} = -35\ \text{kJ/mol} \tag{2}$$

Equation (2) is usually referred to as water-gas shift reaction. It should be mentioned that the steam reforming reaction in Eq. (1) is endothermic and the overall balance of the reaction requires net heat input by the electrochemical reaction. The electrochemical reactions to generate electricity are the oxidation of H_2 and CO

$$H_2 + O^{2-} \rightarrow H_2O + 2e^- \quad \Delta H_{1000\ K} = -248\ \text{kJ/mol} \tag{3}$$

$$CO + O^{2-} \rightarrow CO_2 + 2e^- \quad \Delta H_{1000\ K} = -283\ \text{kJ/mol} \tag{4}$$

The above reactions produce a significant amount of water and heat at the anode during operation.

A three-dimensional computational fluid dynamics (CFD) code is employed for an anode duct of a typical ITSOFC design. Structure of a unit cell and a schematic drawing of the anode duct are shown in Figs. 1(*a*) and 1(*b*). The U, V, and W are the velocity components in the x, y, z directions, respectively. In this study, the porous anode layer is assumed to be homogeneous and characterized by effective parameters and the fuel species in the porous layer are in thermal equilibrium with the solid matrix. The electrochemical reaction appears at the interface between the electrolyte and the porous layer, i.e., the bottom surface in Fig. 1, while the internal reforming reactions are within the porous layer. A constant flow rate $U = U_{\text{in}}$ with a mass fraction of the mixed fuel gas is specified at the inlet of the fuel gas flow duct, while $U = 0$ is specified at the inlet for the interconnect and porous anode layer. Only the right half of the duct is considered by imposing symmetry conditions on the midplane.

2.2 Governing Equations and Source Terms. The governing equations to be solved are the continuity, momentum, energy and species equations. The mass continuity equation is written as

$$\nabla \cdot (\rho_{\text{eff}} \mathbf{v}) = S_m \tag{5}$$

The source term S_m in the above equation accounts for the mass balance due to the electrochemical reactions at the active surface (bottom surface in Fig. 1(*b*))

$$S_m = (J_{H_2} + J_{CO} + J_{H_2O})\frac{A_{\text{active}}}{V} = \left(-\frac{i_{H_2}}{2F}M_{H_2} - \frac{i_{CO}}{2F}M_{CO} + \frac{i_{H_2} + i_{CO}}{2F}M_{H_2O}\right)\frac{A_{\text{active}}}{V} \tag{6}$$

where V refers to control volume, $(i_{H2} + i_{CO})$ is the total current density i passing through the cell, J is the electrochemical reaction related molar flux.

The momentum equation reads

$$\nabla \cdot (\rho_{\text{eff}} \mathbf{v}\mathbf{v}) = -\nabla P + \nabla \cdot (\mu_{\text{eff}} \nabla \mathbf{v}) + S_{di} \tag{7}$$

The inclusion of the source term S_{di} allows Eq. (7) to be valid for both the porous layer and the fuel gas flow duct

$$S_{di} = -(\mu_{\text{eff}} \mathbf{v}/\beta) - \rho_{\text{eff}} B V_i |\mathbf{v}| \tag{8}$$

in which, β is the porous layer permeability, and $\boldsymbol{V}$ represents the volume-averaged velocity vector of the species mixture. For example, the volume-averaged velocity component U in the x direction is equal to εU_p, where ε is the porosity, and U_p is the average pore velocity (or interstitial velocity). The first term on the right-hand side of Eq. (8) accounts for the linear relationship between the pressure gradient and flow rate according to Darcy's law. The second term is the Forchheimer term which takes into account the inertial force effects, i.e., the non-linear relationship between pressure drop and flow rate [7].

It should be noted that the moment equation is formulated to be generally valid for both the fuel gas flow duct and the porous anode, i.e., the source term is zero in the fuel gas flow duct, because the permeability β is infinite. Equation (7) then reduces to the regular Navier-Stokes equation. For the porous anode, the source term Eq. (8) is not zero, and the momentum Eq. (7) with the nonzero source term can be regarded as a generalized Darcy model [7].

The species conservation equations are formulated in a general form,

$$\nabla \cdot (\rho_{\text{eff}} \mathbf{v} Y_i) = \nabla \dot{\mathbf{m}}_i + S_{s,i} \tag{9}$$

where Y_i is the mass fraction of the ith fuel gas species, $\dot{\mathbf{m}}_i$ represents the mass diffusive flux of species in units of $\text{kg}/(\text{m}^2\,\text{s})$, and $S_{s,i}$ the production/consumption rate of the ith fuel species. The above equation is solved for H_2, CH_4, CO, and H_2O, respectively, i.e., for $n-1$ species, where n is the total number of species involved in the fuel gas mixture. The last species (CO_2) can be solved because the sum of the mass fractions equals one.

Mass diffusion is a process leading to equalization of substance concentration or establishing an equilibrium gas distribution that results from random migration of the species. Molecular diffusion occurs as a result of thermal motion of the molecules, and proceeds at a maximum rate in gases, a lower rate in liquids, and at a still lower rate in solids [10]. In the general case, the molecular diffusion flux of the species i is proportional to the concentration gradient and diffusion coefficient. One of the significant challenges in fuel cell modelling is in determining the rate at which the species diffuse and gases convect in the gas flow ducts and porous electrodes. This requires knowledge of multicomponent diffusion in the fuel gas flow ducts, particularly in the porous

layers. In the literature, there are several basic approaches for determining the molar diffusion flux $\dot{\mathbf{n}}_i$ and converting to mass diffusion flux $\dot{\mathbf{m}}_i$ via the species molar mass, i.e., $\dot{\mathbf{n}}_i = \dot{\mathbf{m}}_i / M_i$. Fick's law, represented by $\dot{\mathbf{n}}_i = -\rho D_{i,j} \nabla X_i$ based on binary diffusion coefficient $D_{i,j}$ and molar fraction X_i, is the simplest diffusion model and is typically used in binary or dilute system [10]. A multicomponent extension of Fick's law is sometimes used in the literature as well, e.g., in [11],

$$\dot{\mathbf{n}}_i = -\rho D_{i,j} \nabla X_i + X_i \sum_{i=1}^{n} \dot{\mathbf{n}}_j \tag{10}$$

while the Stefan-Maxwell model is more commonly used in the multicomponent system, as in this study. The diffusion coefficients of species i in the fuel gas flow duct is calculated by the expression based on the binary coefficients [10]

$$D_{A,gm} = \frac{1 - X_A}{X_B/D_{AB} + X_C/D_{AC} + \cdots} \tag{11}$$

where D_A is the diffusion coefficient of the component A in the mixture with $B, C, \ldots, X_A, X_B, X_C$ are the molar fraction of the appropriate species, and D_{AB} and D_{AC} are the diffusion coefficients in the AB and AC binary system, respectively. It is clear that for an n component system, $n(n-1)/2$ binary diffusivities are required.

For the porous layer, molecular diffusion is predominant in the case with large pores, whose size is much bigger than the free-path of the diffusion gas molecules. In this case, the diffusion can be described as above presented for the fuel gas flow duct. Knudsen diffusion occurs in the porous layer with small pores or under low pressure when the mean free-path of molecules is smaller than the pore size, and the molecules collide with the walls more often than between themselves. In order to calculate the Knudsen diffusion flux, the coefficient $D_{i,k}$ is calculated based on the free molecule flow theory [10]

$$D_{i,k} = \frac{2}{3} r_e v_i = \frac{2}{3} r_e \left(\frac{8 \Re T}{\pi M_i} \right) \tag{12}$$

in which r_e is the effective radius and v_i is the average molecular speed of the ith fuel species. To account for the reduction in the cross-sectional area and the increased diffusion length due to the tortuous paths of real pores in the porous anode, the effective diffusion coefficient can be evaluated [9,10]

$$D_{i,\text{eff}} = \frac{\varepsilon}{\tau} \left(\frac{D_{i,gm} \times D_{i,k}}{D_{i,gm} + D_{i,k}} \right) \tag{13}$$

where ε is the porous anode porosity, and τ is tortuosity. The most common anode is based on nickel/zirconia cermet which can provide sufficient activity for the steam reforming and water-gas shift reactions without the need for any additional catalyst [9]. There exist various reaction kinetics and rate/equilibrium constants reported in the literature for both the steam reforming and water-gas shift reactions. However, based on extensive reviews in [8,9], it can be found that the rate data presented in the literature varies greatly due to the use of different material structures and different amount of catalyst. In this study, the following reaction rates are employed to express the kinetic rates of absorption or production of the fuel gas species, based on partial pressure, temperature, and species compositions

$$R_r = k_r^+ p_{\text{CH}_4} p_{\text{H}_2\text{O}} - k_r^- p_{\text{CO}} (p_{\text{H}_2})^3 \tag{14}$$

$$R_s = k_s^+ p_{\text{CO}} p_{\text{H}_2\text{O}} - k_s^- p_{\text{CO}_2} p_{\text{H}_2} \tag{15}$$

in which, k^+ and k^- are velocity constants of the forward and backward reactions, p partial pressure. Then, $S_{s,i}$ in Eq. (9) reads

$$S_{s,\text{H}_2} = (3R_r + R_s) M_{\text{H}_2};\ S_{s,\text{CH}_4} = -R_r M_{\text{CH}_4}$$

$$S_{s,\text{H}_2\text{O}} = (-R_r - R_s) M_{\text{H}_2\text{O}};\ S_{s,\text{CO}} = (R_r - R_s) M_{\text{CO}} \tag{16}$$

The energy equation can be expressed as

$$\nabla \cdot (\rho_{\text{eff}} c_{p,\text{eff}} \mathbf{v} T) = \nabla \cdot \left(k_{\text{eff}} \nabla T - \sum_{i=1}^{n} \dot{\mathbf{m}}_i h_i \right) + S_T \tag{17}$$

Equation (17) balances the convected energy, the heat conduction through the solid and the fuel gas mixture (heat conduction), the energy due to fuel gas species diffusion, and a source term S_T. In Eq. (17) h_i is the partial enthalpy of the ith species and is obtained from [9]:

$$h_i = h_{\text{form},i} + \int_{T_0}^{T} c_{pi}(T) dT \tag{18}$$

where $h_{\text{form},i}$ is the specific enthalpy of formation of the ith fuel species at $T = T_0 = 298.15$ K. The heat source term S_T in Eq. (17) is associated with the steam reforming and water-gas shift reactions,

$$S_T = \sum_i R_i \Delta h_{\text{reaction},i} \tag{19}$$

where R_i is the internal reforming reaction related mole fluxes, and $\Delta h_{\text{reaction},i}$ is the reaction enthalpy. In the equations above, all thermal-physical and transport parameters with subscript eff are the effective ones, and reduce to the values of the fuel gas mixture in the fuel gas flow duct based on the fuel species composition. However, for the porous anode the effective density is simply evaluated by ρ_f of the fuel gas mixture ($H_2 + CH_4 + CO + H_2O + CO_2$), while, the effective transport parameters, such as thermal conductivity k_{eff} and specific heat $c_{p,\text{eff}}$, are estimated by considering the porous layer effects

$$k_{\text{eff}} = \varepsilon k_f + (1 - \varepsilon) k_s \tag{20}$$

$$c_{p,\text{eff}} = \varepsilon c_{p,f} + (1 - \varepsilon) c_{p,s} \tag{21}$$

2.3 Internal Reforming Reaction Kinetics. As for the kinetics of the natural gas reforming reaction on nickel cermet SOFC anodes, extensive reviews can be found in [8,9]. It is common to employ the forward kinetic reforming reactions in the following form:

$$k^+ = k_0 F(p_i) \exp\left(-\frac{E_a}{\Re T} \right) \tag{22}$$

where $\Re$ is the universal gas constant with unit J/(mol K), F is the function of the species partial pressure, while E_a stands for the activation energy, and k_0 is the pre-exponential constant. It is revealed that the first order kinetic expression is considered typical of direct internal reforming reaction in SOFC performance [8]. The following expressions employed in [9] are adopted in this study:

$$k_r^+ = 2395 \exp(-231266/\Re T) \tag{23}$$

$$k_s^+ = 0.0171 \exp(-103191/\Re T) \tag{24}$$

The backward kinetics k_r^- and k_s^- can be determined based on the following equilibrium constants K_e for the two reactions

$$K_{er} = \frac{k_r^+}{k_r^-}$$

$$K_{es} = \frac{k_s^+}{k_s^-} \tag{25}$$

which are functions of temperature given by the following empirical equations [9]:

$$K_{er} = 1.0267 \times 10^{10} \times \exp(-0.2513Z^4 + 0.3665Z^3 + 0.5810Z^2 - 27.134Z + 3.27770) \tag{26}$$

$$K_{es} = \exp(-0.2935Z^3 + 0.6351Z^2 + 4.1788Z + 0.3169) \quad (27)$$

$$Z = \frac{1000}{T} - 1 \quad (28)$$

2.4 Boundary and Interface Conditions. Based on the ITSOFC function, the thermal and fuel gas mass concentration/flux boundary conditions at the walls are specified as follows, i.e., at the bottom wall ($y=0$):

$$U = V - V_m = W = 0$$

$$q_b = -k_{\text{eff}}\frac{\partial T}{\partial y}$$

$$J_i = -\rho_{\text{eff}} D_{i,\text{eff}}\frac{\partial Y_i}{\partial y} (i = \text{H}_2, \text{CO}, \text{and } \text{H}_2\text{O})$$

$$\text{and } J_i = 0 \quad (i = \text{CH}_4) \quad (29)$$

at the top and side walls

$$U = V = W = 0, \quad q = 0, \quad J_i = 0 \quad (30)$$

at the midplane ($z=a/2$)

$$\frac{\partial U}{\partial z} = \frac{\partial V}{\partial z} = W = \frac{\partial T}{\partial z} = \frac{\partial Y_i}{\partial z} = 0 \quad (31)$$

In the present investigation, the interfacial boundary conditions, commonly employed in the literature, are applied for the continuity of velocity, shear stress, temperature, heat flux, mass fraction and flux

$$U_- = U_+, (\mu_{\text{eff}}\partial U/\partial y)_- = (\mu_f \partial U/\partial y)_+ \quad (32)$$

$$T_- = T_+, (k_{\text{eff}}\partial T/\partial y)_- = (k_f \partial T/\partial y)_+ \quad (33)$$

$$Y_{i-} = Y_{i+}, (\rho_{\text{eff}} D_{i,\text{eff}}\partial Y_i/\partial y)_- = (\rho_f D_{i,gm}\partial Y_i/\partial y)_+ \quad (34)$$

Here subscript + (plus) stands for fluid side, − (minus) for porous layer side. Moreover, the thermal interfacial condition, Eq. (33), is also applied at an interface between the porous anode and the solid current interconnect with k_s instead of k_f.

3 Numerical Solution Methdology

A three-dimensional CFD code is further developed and employed to solve the governing Eqs. (5), (7), (9), and (17), together with the boundary conditions (29)–(31) and interfacial conditions (32)–(34). The code is further developed based on a general purpose finite-volume technique with boundary fitted coordinates for solving the differential equations. The Cartesian coordinate system in the physical space is replaced by a general nonorthogonal coordinate system. The momentum equations are solved for the velocity components on a nonstaggered grid arrangement. The Rhie-Chow interpolation method is used to compute the velocity components at the control volume faces. Algorithms based on the TDMA and a modified SIP are employed for solving the algebraic equations. In this study, the convective terms are treated by the QUICK scheme, while the diffusive terms are treated by the central difference scheme. The SIMPLEC algorithm handles the linkage between velocities and pressure.

As shown above, the equations needed for the calculation are coupled by the current density, temperature, fuel species partial pressure/concentration via source terms and variable physical/transport properties. It should be noted that the source term in Eq. (5) is zero in most of the regions, and nonzero only in the regions neighboring boundaries, where mass transfer caused by the electrochemical reaction occurs (the bottom wall in Fig. 1(*b*)). It is clear that no gas flow is present in the solid interconnect. Equations (5), (7), and (9) are then blocked out and only the heat conduction equation, derived from the energy Eq. (17), is solved for this domain. As mentioned earlier, the physical/transport properties of the fuel gas mixture are variable. These parameters depend on the position in the duct, and the fuel species mass fraction and temperature as well. All the parameters are calculated and updated during iterations of the calculation.

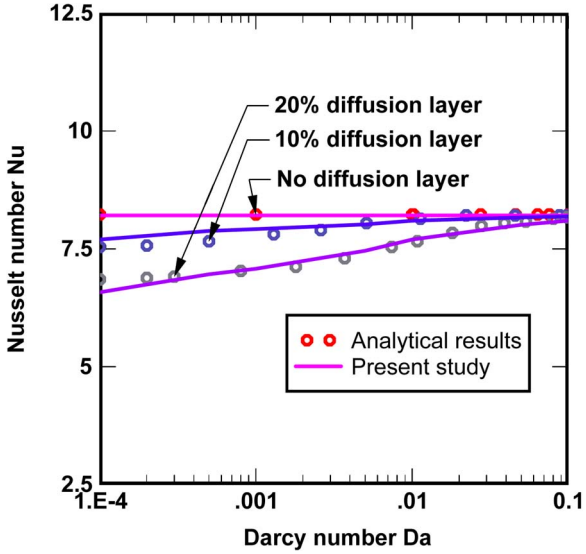

Fig. 2 Fully developed Nusselt number Nu variation in a parallel plate duct with Darcy number ($\text{Da}=\beta/h^2$), compared to the analytical ones from [12]

In this investigation, a uniform grid point distribution in the cross section is applied. To obtain finer meshes in the entrance region of the duct, a nonuniform distribution of grid points with an expansion factor is implemented for the main flow direction. Various values of the expansion factor have been checked and 1.01 was found to be sufficient to achieve grid independent solutions.

In order to evaluate the performance of the numerical method and code, test calculations considering grid sensitivity, code performance and validation were carried out. It is clear that the predictions do not change significantly in terms of fuel species distributions, when the number of grid points is increased beyond $70\times70\times50$ (70×50 for the cross section, 70 for the main flow direction). Calculations have been carried out for fully developed conditions in a parallel plate duct for various thickness of the porous layer and the same boundary conditions of constant heat flux on the walls. The comparison in Fig. 2 shows that the computed values of Nusselt numbers Nu agree well with the analytical ones in [12].

4 Results and Discussion

Parameters of ITSOFCs and the porous anode configuration, appearing in the common literature, are applied as a base case in this study. Duct geometries are employed as follows: length of the duct $L=20$ mm; width of the porous layer $a=2$ mm, and its thickness $h_p=2$ mm; while the width of the flow duct is $b=1$ mm, and its height $h_d=1$ mm. Fuel gas inlet conditions are: temperature $T_{\text{in}}=800°\text{C}$, partially (30%) prereformed methane/steam mixture with: $\text{Re}_{\text{in}}=50$, molar concentration $X_{\text{H}_2}:X_{\text{CH}_4}:X_{\text{CO}}:X_{\text{H}_2\text{O}}:X_{\text{CO}_2}=0.284:0.171:0.028:0.473:0.044$. In the porous layer, typical values are employed for porosity $\varepsilon=0.5$, tortuosity $\tau=3$, and permeability $\beta=2\times10^{-10}$ m^2. The binary diffusion coefficients of the fuel species are shown in Table 1. In this study, a constant total current density $i=0.6$ A/cm^2 is prescribed, however this limitation will be released in future investigations when the electrolyte

Table 1 Binary diffusivity of the *i*th fuel gas species at T =1123.15 K, p=1.013 bar [4,13]

i/j	$D_{i,j}$ (m^2/s)	i/j	$D_{i,j}$ (m^2/s)
CH_4/CO	3.47×10^{-5}	CO/H_2	11.92×10^{-5}
CH_4/H_2O	4.30×10^{-5}	CO/CO_2	2.59×10^{-5}
CH_4/H_2	11.04×10^{-5}	H_2O/H_2	14.10×10^{-5}
CH_4/CO_2	2.88×10^{-5}	H_2O/CO_2	3.38×10^{-5}
CO/H_2O	4.15×10^{-5}	H_2/CO_2	10.23×10^{-5}

is included. It should be noted that all the results presented hereafter are for the base case condition unless otherwise stated, such as sensitive parameter studies.

Both the steam reforming reaction and the shift reaction rates are shown in Figs. 3(*a*) and 3(*b*), respectively. It is found that both reactions are strong at the interface and the entrance regions within the porous layer close to the fuel flow duct (with big reaction rate value). No reactions can be observed in the rest of the porous anode, particularly after a certain distance downstream the inlet. The distance for this specific case is about half the duct length.

The steam reforming reaction rates are plotted in Fig. 4 for the cross section at the stations of the inlet, the one-fourth and the half length from the inlet, respectively. It is found that, in a cross section, R_r has maximum values in the regions close to the fuel flow duct, and small values or even no reaction appear in the rest of the porous anode. It is so because there is strong fuel gas permeation to the porous anode due to large pressure gradients [5]. It is also observed that these maximum values decrease along the main flow direction, i.e., the maximum reaction rates are about 15, 10, and 5.4 mol/(m^3 s) for Figs. 4(*a*)–4(*c*), respectively. There is no steam reaction for almost all the porous anode at the station of the half length from the inlet, as shown in Fig. 4(*c*), because the methane is completely reformed as discussed in the following sections. It should be mentioned that a similar trend is found for the water-gas shift reaction rate distribution (not shown in this paper).

Axial velocity contours (U/U_{in}) and the temperature profile are presented for an ITSOFC anode duct in Fig. 5. As mentioned above, gas flow and heat transfer in the composite ducts are affected by the internal reforming reactions in the porous layer and the electrochemical reactions close to the active surface. Due to the permeation and mass generation/consumption effects, the uniform distribution and the symmetry of the axial velocity associated with a pure forced duct flow does no longer exist, and the position of the maximum contour values shifts away from the central plane (y/h=0.625 in Fig. 5(*a*)). More mass is permeated into the porous anode layer at the entrance area because the largest pressure gradient between the flow duct and the porous layer occur here [5]. As a consequence, part of the boundary is shifted into

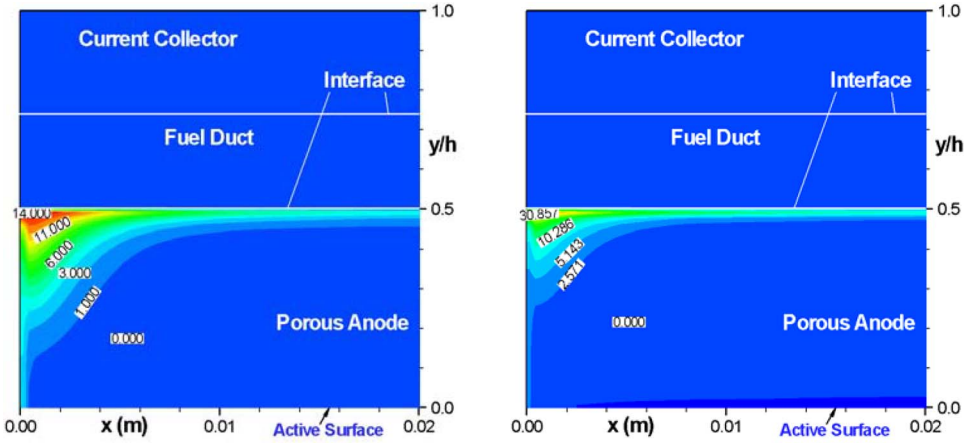

Fig. 3 Distribution of (*a*) steam reforming reaction rate R_r; and (*b*) shift reaction rate R_s along main flow direction at the base case

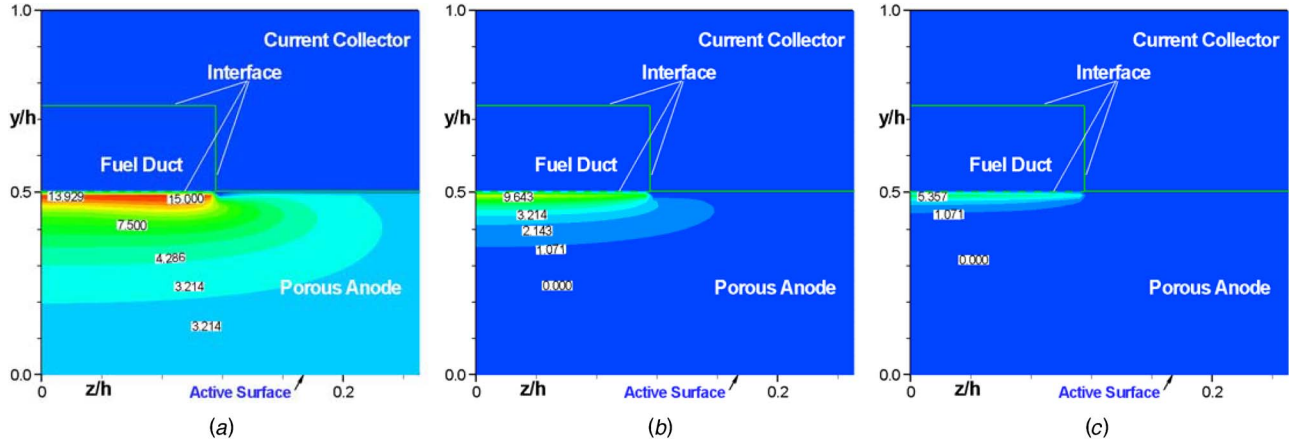

Fig. 4 Cross-sectional steam reforming reaction rate R_r distribution at (*a*) the inlet; (*b*) the one-fourth; and (*c*) the half length from the inlet of an ITSOFC duct

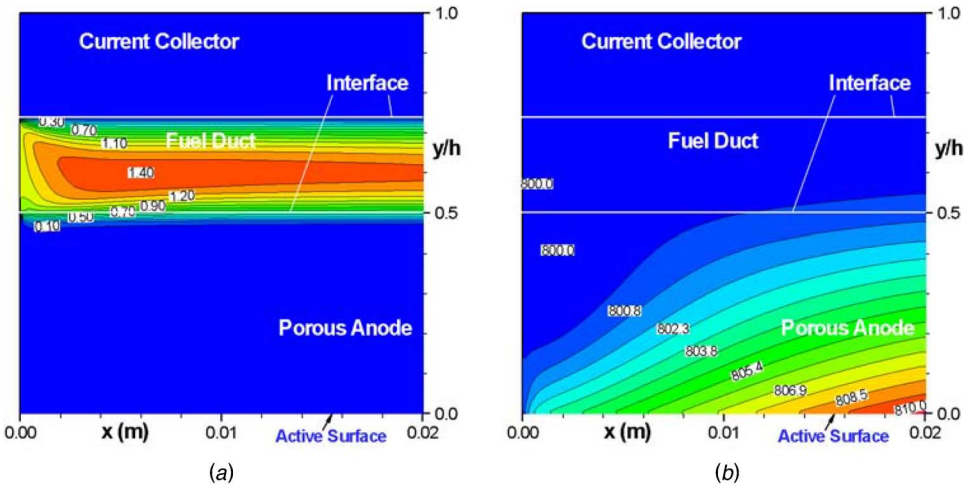

Fig. 5 Distribution of (*a*) dimensionless axial velocity contours (U/U_{in}); and (*b*) temperature along the main flow stream of an ITSOFC anode duct at the base case condition

the porous anode layer, which can be verified by a change of the boundary layer thickness close to the interface in Fig. 5(*a*). Because the pressure in the fuel flow duct will fall due to friction, a decreased pressure gradient along the main stream is expected. Consequently, gas permeation decreases and becomes weaker. It is clear that the axial velocity magnitude of the fuel mixture decreases rapidly in the porous layer. It is clear that the temperature increases steadily along the main flow direction in Fig. 5(*b*). The variation in temperature distribution can also be observed in the vertical direction with a slightly larger value close to the active surface. These are created by the heat generation due to the electrochemical reactions close to the active surface.

The internal reforming reaction can be found in Fig. 6(*a*) by the methane mass fraction distribution in the anode duct, particularly in the porous anode. A large amount of CH_4 is reacted in the interface region of the porous layer close to the fuel duct, which is reflected by a sharp decrease of CH_4 mass concentration. This region is confined only up to around 200–300 μm into the anode porous layer at most of the stations along the main flow stream, except at the inlet areas where the reactions take place more deeply into the porous anode. There is hardly any methane reaching the active surface after the first 10% of the duct length, see Fig. 6(*a*). On the other hand, the active surface is sufficiently supplied with H_2 resulting from both the steam reforming and water-gas shift reactions. Moreover, the H_2 mass concentration is affected by the mass consumption from the electrochemical reactions, as shown in Fig. 6(*b*).

CH_4 mass fraction profiles are plotted in Fig. 7 for the cross section at the stations of the inlet, the one-fourth and the half length from the inlet, respectively. It is found that, in a cross section, the CH_4 mass fraction has minimum values close to the electrochemical active surface (bottom surface in Fig. 7), which is caused by the reforming reaction mentioned above. Almost uniformly distributed mass concentrations can be found in both the fuel flow duct and the porous anode. However, a bigger value has been predicted in the porous anode close to the side wall. It should be mentioned that the CH_4 profile at the exit is similar to that at the half length from the inlet in Fig. 7(*c*), and then not shown in this study. It is verified that, just after a short distance from the inlet, the methane is completely reformed before reaching the active surface, and no CH_4 can be found in most regions of the porous anode after the one-fourth length downstream the entrance (see Fig. 7(*b*)).

CO and H_2O mass fraction profiles along the main flow stream are shown in Figs. 8(*a*) and 8(*b*), respectively. It is found that there is a small CO concentration within the porous anode close to the flow duct at the entrance region due to the CO consumption by

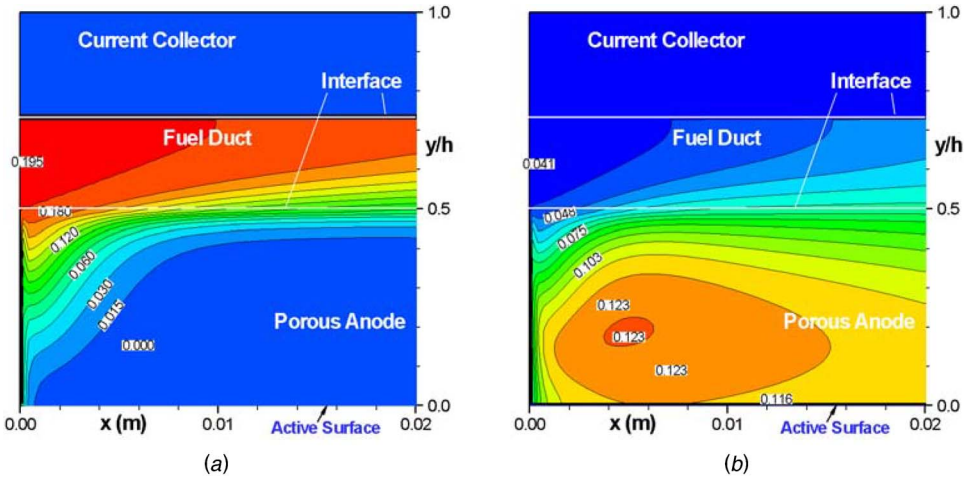

Fig. 6 Mass concentration of (*a*) CH_4; and (*b*) H_2 along main flow direction of an ITSOFC anode duct at the base case condition

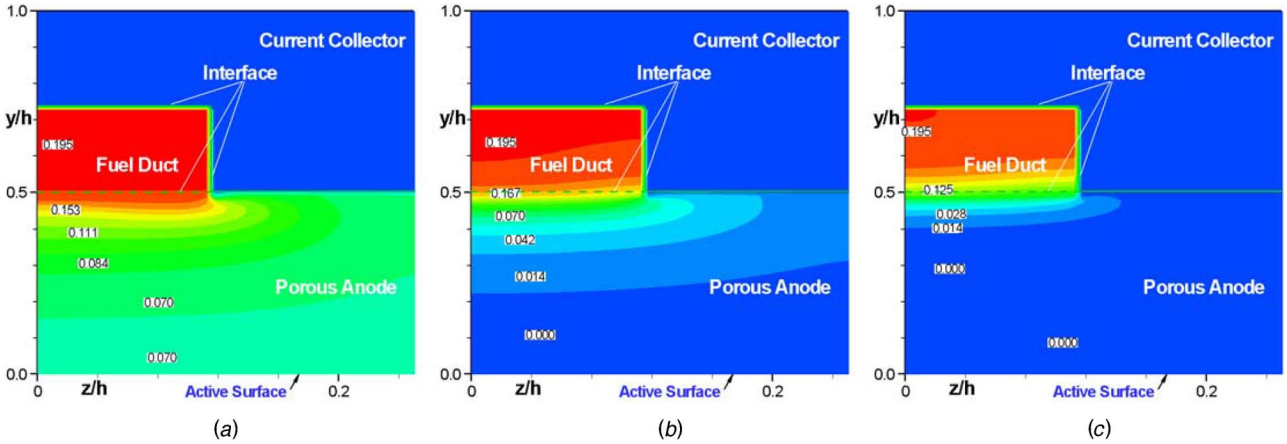

Fig. 7 Cross-sectional CH_4 mass concentration distribution at (*a*) the inlet; (*b*) the one-fourth; and (*c*) the half length from the inlet of an ITSOFC duct

the fast water-shift reaction (as revealed in Fig. 3). It is found that the concentration gradients are bigger for the regions where the reforming reaction and the electrochemical reactions appear, i.e., the areas close to the flow duct and the active surface. It should be noted that the CO concentration changes in a small range (between 2–9%). It is observed that H_2O is consumed in the porous anode by both the steam reforming and the water-gas shift reactions. For this reason, mass fractions of H_2O decrease along the main flow direction and to the active surface. However, generation of H_2O by the electrochemical reactions affects the H_2O distribution as well, particularly for the area close to the active surface. A minimum value is found in the porous anode close to the duct exit.

Sensitive studies have also been conducted for the operating conditions and the configuration parameters. Figure 9 shows the CH_4 mass fraction profiles for various cell operating temperatures. It is found that the CH_4 mass concentration decreases faster in both the main flow and the vertical directions at higher temperature, i.e., 900°C in Fig. 9(*a*), if compared to the base case 800°C in Fig. 6(*a*) and 700°C in Fig. 9(*b*). It is clear that all methane is reacted in a very small region of the porous anode close to the inlet at the higher temperature. This is so because the steam reforming reaction depends on the temperature, i.e., a higher temperature causes a faster reaction. On the other hand, methane is not fully reformed at the low temperature, as shown in Fig. 9(*b*), and reaches the active surface. It is more significant if the temperature goes further down to 600°C, as shown in Fig. 9(*c*). As for this specific case, there is a limitation in reducing the operating temperature in terms of internal reforming reactions.

Figure 10 shows the temperature distribution for various cell operating temperatures. By comparing Fig. 10 with Fig. 5(*b*), it is found that there is a similar trend for the temperature profiles. The temperature increases along the main flow stream and to the active surface, as a result of the electrochemical reactions. The only exception is that in Fig. 10(*b*) a lower temperature can be found in the areas corresponding to the fast internal reforming reactions, when the operating temperature is higher. In this case, an extra temperature gradient is created.

Figure 11 shows the impact of the porous anode permeability on the fuel gas flow. It is noted from Fig. 11(*a*) that, by decreasing the permeability, fuel gas permeation to the porous anode is small, i.e., the axial velocity is zero for the most regions of the porous anode. Furthermore, the velocity in the fuel flow duct is similar to the parabolic one associated with the pure duct flow. This is so because the permeability is a term used for the conductivity of the porous medium with respect to permeation by a fluid. It is known that a small permeability of a porous layer allows less gas to pass at the same pressure gradient. As for a big permeability in Fig. 11(*b*), more fuel gas is permeated from the flow duct, and as a result the gas convection can be clearly found with certain veloci-

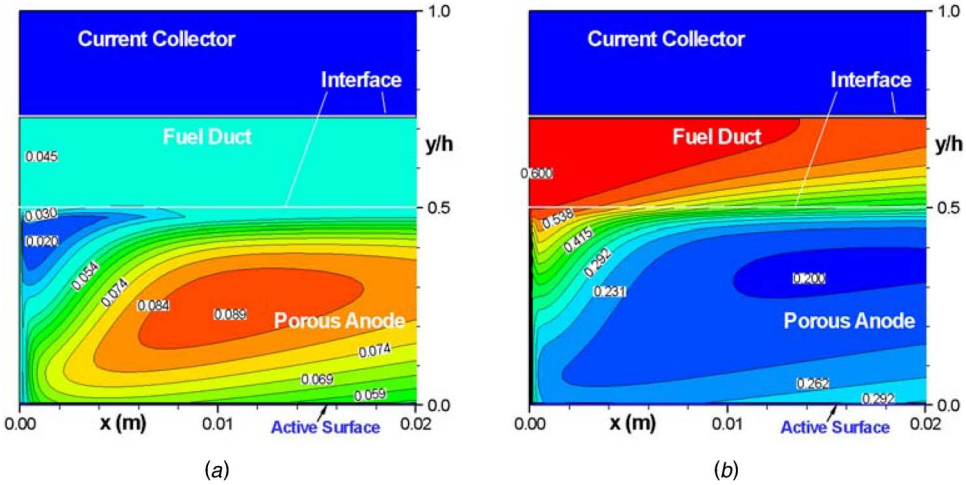

Fig. 8 (*a*) CO; and (*b*) H_2O mass concentration distribution along main flow direction of an ITSOFC anode duct at the base case condition

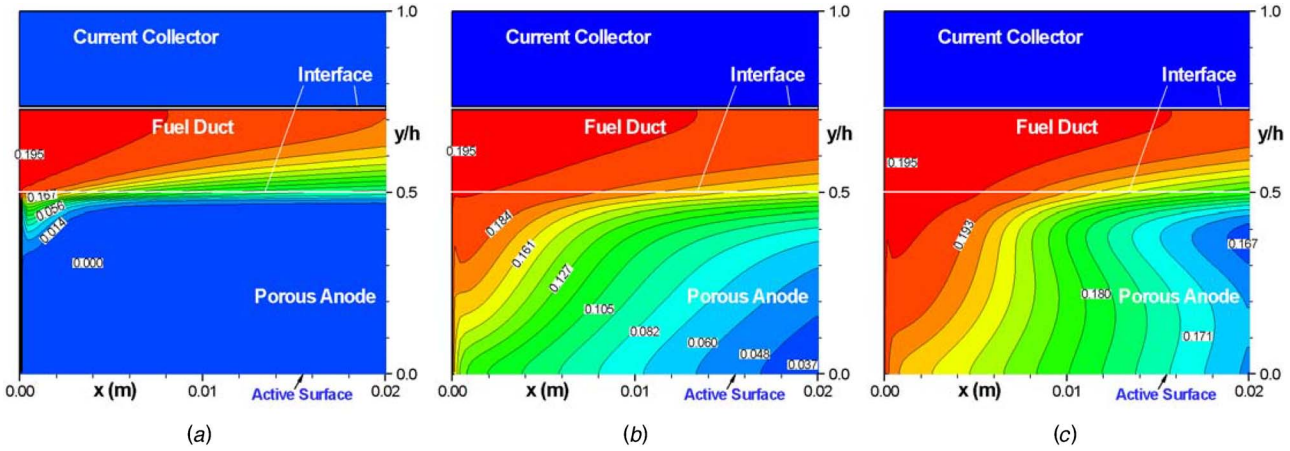

Fig. 9 CH_4 distribution at (*a*) 900°C; (*b*) 700°C; and (*c*) 600°C along the main flow direction of an ITSOFC anode duct

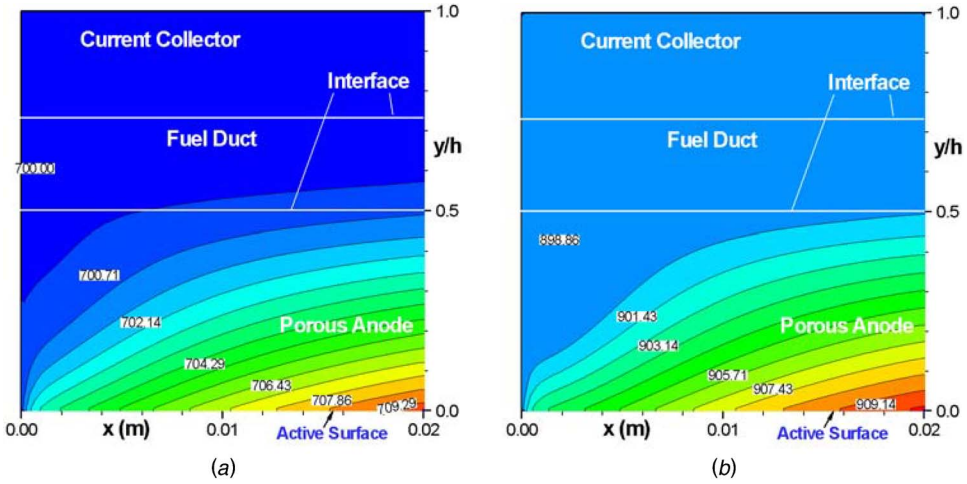

Fig. 10 Temperature distribution at (*a*) 700°C and (*b*) 900°C along the main flow direction of an ITSOFC anode duct

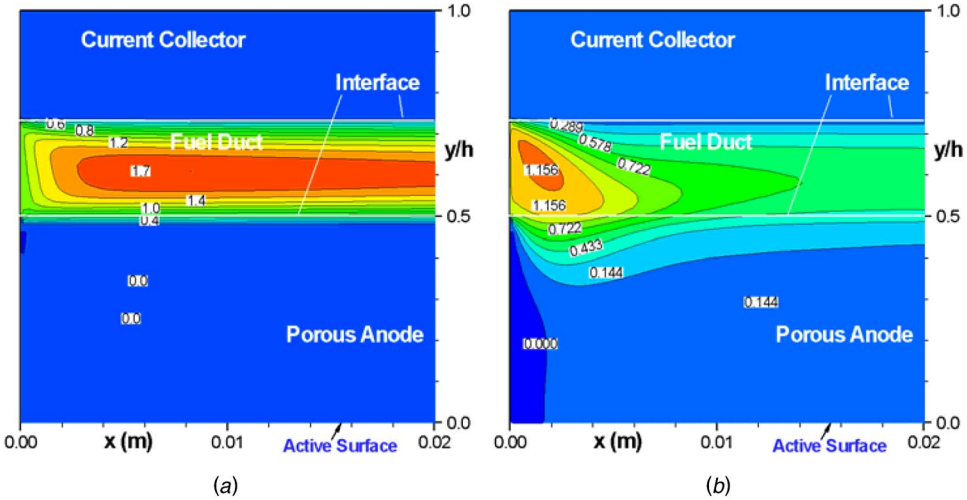

Fig. 11 Dimensionless axial velocity contours distribution at (*a*) $\beta=2.0\times10^{-11}$; (*b*) $\beta=2.0\times10^{-9}$ along the main flow direction of an ITSOFC anode duct

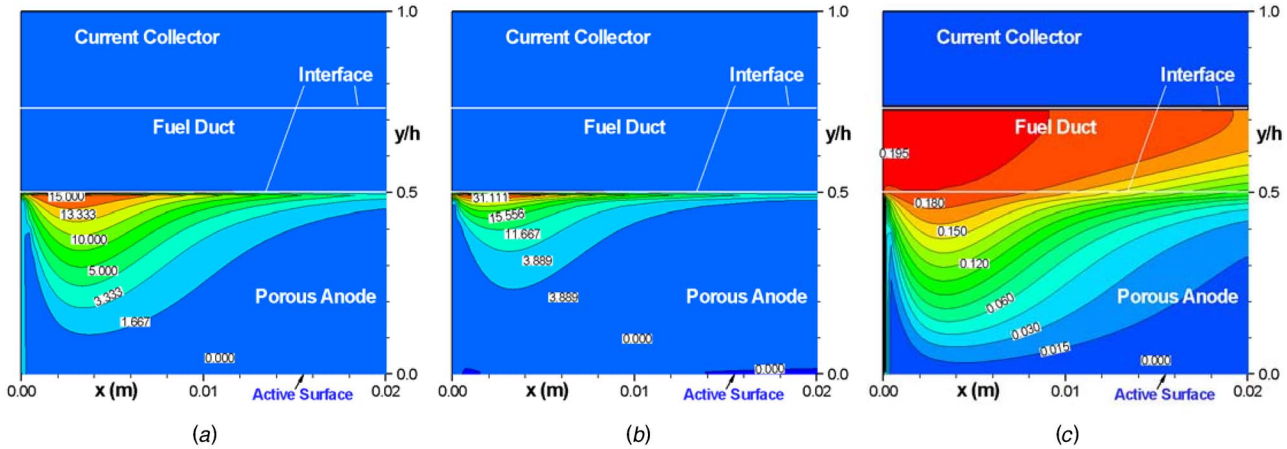

Fig. 12 (*a*) Steam reforming reaction rate R_r; (*b*) water-gas shift reaction rate R_s; (*c*) CH_4 distribution at $\beta=2.0\times10^{-9}$ along the main flow direction of an ITSOFC anode duct

ties in the porous anode. Consequently, more significant impacts on the change of the axial velocity distribution are expected for both the flow duct and the porous anode, when the permeability is higher.

As a consequence, more significant impacts on the internal reforming reactions and fuel gas distribution are expected for the case of the larger permeability. From Figs. 12(*a*) and 12(*b*), it is found that both the steam reforming reaction and the water-gas shift reaction happen deeply in the porous anode. As for this case, utilization of catalytic surfaces in the porous anode can be expected, as verified by the CH_4 distribution in Fig. 12(*c*).

5 Conclusions

A fully three-dimensional CFD method has been further developed to simulate and analyze the gas flow and heat transfer processes involving various chemical reactions in a thick anode duct of ITSOFCs. Momentum and heat transport together with gas species equations have been solved for a composite domain by coupled source terms and variable thermophysical and transport properties of the fuel gas species. The model offers the possibilities of determining various parameter distribution profiles, by taking into account the internal reforming reactions and the electrochemical reactions.

Based on the predicted results from this study it is found that, at most regions apart from the cell inlet, the internal reforming reactions are confined in a thin porous anode layer close to the fuel flow duct. Transport processes of the fuel gas species and temperature distribution are affected by both the internal reforming reactions and the electrochemical reaction. Higher temperature is favorable for faster internal reforming reactions, while a larger porous anode permeability has more significant effects on the transport processes.

Acknowledgment

The current research is financially supported by the National Fuel Cell Programme by the Swedish Energy Agency (STEM).

Nomenclature

A_{active} = surface area of control volume at active site, m^2
a = width of porous layer, m
B = inertial coefficient
b = width of flow duct, m
c_p = specific heat capacity, J/(kg K)
D = molar diffusion coefficient of fuel gas species, m^2/s
E_a = activation energy, kJ/mol
H = enthalpy, kJ/mol
h = overall height of the duct, m
h_d = height of the duct, m
h_p = thickness of porous layer, m
J = electrochemical reaction related molar flux, $mol/(m^2\ s)$
K_e = equilibrium constants, Pa^2
k = thermal conductivity, W/(m K); reaction rate constant, $mol/(m^3\ Pa^2\ s)$
k_0 = pre-exponential constant
M = molecular weight of species, kg/mol
$\dot{\mathbf{m}}$ = mass diffusion flux, $kg/(m^2\ s)$
$\dot{\mathbf{n}}$ = molar diffusion flux, $mol/(m^2\ s)$
n = total number of species
P = pressure, Pa
q = heat flux, $W/(m^2)$
R = internal reforming reaction rate, $mol/(m^3\ s)$
$\mathfrak{R}$ = gas constant, kJ/(mol K)
Re = Reynolds number (UD_h/ν)
r_e = effective radius, m
S = source term
T = temperature, °C
$\mathbf{v}$ = velocity vector, m/s
V_i = velocity components in x, y, and z directions, respectively, m/s
X = molar fraction of fuel species
Y = mass fraction of fuel species
x,y,z = Cartesian coordinates

Greek Symbols

β = permeability of porous layer (m^2)
ε = porosity
μ = dynamic viscosity, kg/(m s)
ν = kinematic viscosity, m^2/s
ρ = density, kg/m^3
τ = tortuosity

Superscripts

$+$ = forward reaction
$-$ = reverse reaction

Subscripts

di = diffusion layer
eff = effective parameter
f = fuel gas mixture
CH_4 = methane
CO = hydrocarbon monoxide
CO_2 = hydrocarbon dioxide

e = equilibrium
gm = fuel gas mixture
H_2 = hydrogen
H_2O = water
in = inlet
k = Knudsen diffusion
m = mass transfer
p = permeation
r = steam reforming reaction
s = solid wall; shift reaction; species

References

[1] Virkar, A. V., Chen, J., Tanner, C. W., and Kim, J. W., 2000, "The Role of Electrode Microstructure on Activation and Concentration Polarizations in Solid Oxide Fuel Cells," Solid State Ionics, **131**, pp. 189–198.

[2] Yakabe, H., Hishinuma, M., Uratani, M., Matsuzaki, Y., and Yasuda, I., 2000, "Evaluation and Modeling of Performance of Anode-Supported Solid Oxide Fuel Cell," J. Power Sources, **86**, pp. 423–431.

[3] Lehnert, W., Meusinger, J., and Thom, F., 2000, "Modelling of Gas Transport Phenomena in SOFC Anodes," J. Power Sources, **87**, pp. 57–63.

[4] Ackmann, T., Haart, L. G. J., Lehnert, W., and Thom, F., "Modelling of Mass and Heat Transport in Thick-Substrate Thin-Electrolyte Layer SOFCs," in *Proceedings of the 4th European Solid Oxide Fuel Cell Forum 2000*, Lucerne/Switzerland, pp. 431–438.

[5] Yuan, J., Rokni, M., and Sundén, B., 2003, "Three-Dimensional Computational Analysis of Gas and Heat Transport Phenomena in Ducts Relevant for Anode-Supported Solid Oxide Fuel Cells," Int. J. Heat Mass Transfer, **46**, pp. 809–821.

[6] Yuan, J., Rokni, M., and Sundén, B., 2003, "Gas Flow and Heat Transfer Analysis for an Anode Duct in Reduced Temperature SOFCs," in *Fuel Cell Science, Engineering and Technology*, R. K. Shah and S. G. Kandlikar, eds., pp. 209–216, FUELCELL2003–1721, ASME.

[7] Yuan, J., Faghri, M., and Sundén, B., 2005, "On Heat and Mass Transfer Phenomena in PEMFC and SOFC and Modeling Approaches," in *Transport Phenomena in Fuel Cells*, B. Sundén, and M. Faghri, eds., WIT Press.

[8] Aguiar, A., Adjiman, C. S., and Brandon, N. P., 2004, "Anode-supported Intermediate Temperature Direct Internal Reforming Solid Fuel Cell. I: Model-based Stead-state Performance," J. Power Sources, **138**, pp. 120–136.

[9] Haberman, B. A., and Young, J. B., 2004, "Three-dimensional Simulation of Chemically Reacting Gas Flows in the Porous Support Structure of an Integrated-planar Solid Oxide Fuel Cell," Int. J. Heat Mass Transfer, **47**, pp. 3617–3629.

[10] Mostinsky, I. L., 1996, "Diffusion Coefficient," in *International Encyclopedia of Heat and Mass Transfer*, Hewitt, G. F., Shires, G. L., and Polezhaev, Y. V., eds., CRC Press, Florida.

[11] Ferguson, J. R., Fiard, J. M., and Herbin, R., 1996, "Three-dimensional Numerical Simulation for Various Geometries of Solid Oxide Fuel Cells," J. Power Sources, **58**, pp. 109–122.

[12] Alazmi, B., and Vafai, K., 2001, "Analysis of Fluid Flow and Heat Transfer Interfacial Conditions Between a Porous Medium and a Fluid Layer," Int. J. Heat Mass Transfer, **44**, pp. 1735–1749.

[13] Borgnakke, C., and Sonntag, R. E., 1997, *Thermodynamic and Transport Properties*, Wiley, New York.